Facultad de Ciencias

Sección de Física

Trabajo de Fin de Grado

Characterization of the parameters of an infrared astronomical detector. Application in EMIR.

Francisco José Rodríguez Cerezo

Tutor: **Dr. Francisco Garzón López**

July 2021

Abstract

This thesis presents and examines the characteristics of a detector for astronomical observations operating in the infrared range. This detector is part of an instrument located on the Gran telescopio de Canarias (GTC) at the observatory of El Roque de Los Muchachos, on the island of La Palma. It is a multi-object near-infrared spectrograph (EMIR). This project analyses in depth the operation of the instrument in order to understand the behaviour of the sensor in the face of various factors inherent to it. Such as reading noise, dark current, linearity and detector gain.

Abstract

Este trabajo presenta y examina las características de un detector para observaciones astronómicas que opera en el rango infrarrojo. Este detector forma parte de un instrumento situado en el Gran telescopio de Canarias (GTC) en el observatorio de El Roque de Los Muchachos, en la isla de La Palma. Se trata de un espectrógrafo multiobjeto del infrarrojo cercano (EMIR). En este proyecto se analiza en profundidad el funcionamiento del instrumento para entender el comportamiento del sensor ante diversos factores inherentes al mismo. Como el ruido de lectura, la corriente de oscuridad, la linealidad y la ganancia del detector.

Contents

Chapter 1

Introduction

This chapter will provide the reader with a background on the importance of instrumentation development in astrophysics. It will also situate EMIR in this field and describe the general objectives of this study as well as the methodology of the work.

Este capítulo proporcionará al lector una visión general de la importancia del desarrollo de la instrumentación en astrofísica. También situará a EMIR en este campo y describirá los objetivos generales de este estudio, así como la metodología del trabajo.

1.1 Instrumentation in astrophysics

The history of astronomy is as old as the history of mankind, since its origins it has sought to give meaning to existence. Almost all ancient civilizations developed their own religion and cosmogony, with the intention of explaining the origin and functioning of the world or foreseeing its future based on the observation of the celestial vault and the movement of the stars. Assyrians, Chaldeans, Greeks, Romans, Phoenicians, Egyptians, Renaissance Europe, Enlightenment Europe... These are some of the cultures in which astronomy has been relevant but always linked to the observation of the human eye.

It was not until 1610 when Galileo resolved the satellites of Jupiter with his telescope and the revolution of instrumentation in astronomy began. In the 19th century, astronomical photography appeared and we began to be able to integrate

(accumulate observation time beyond what our eyes can see). Then solid-state detectors in the 1950s and so on to the present day where astronomy does not depend solely on observation and different branches of this science have taken place thanks to technology and the instrumental revolution.

1.2 EMIR's interest

EMIR is one of the first multi-object infrared spectrographs. It operates between $0.9\mu m$ and $2.5\mu m$ using cryogenic configurable multi-slit masks [1]. The importance and interest of observing in the infrared is due to the fact that radiation in this range is less absorbed by cosmic dust, making it possible to observe hidden regions in the visible range of the spectrum. In addition, the infrared provides access to many spectroscopic lines. The reconfigurable slit system (CSU) allows one to take spectra of up to 53 objects simultaneously. We cannot use the 55 slits, due to the vignetting produced in the location of the first and last slit.

The EMIR design was largely determined by the requirements of its main scientific driver, the study of distant, faint galaxies. Being a common-user instrument, however, it has been designed to meet many of the broadest expectations of the astronomical community. It is, therefore, a versatile instrument that will accomplish a wide variety of scientific projects in extragalactic, stellar and Solar System astronomy [2].

1.3 EMIR's detector description

The EMIR's detector is divided into 4 quadrants, each with a 1024×1024 pixels format, resulting in a total sensor resolution of 2048×2048. In turn, each of these quadrants is divided into 8 channels of 128×1024 or 1024×128 as appropriate, since the quadrants are rotated 90^{o} with respect to the previous one, as shown in the following figure.

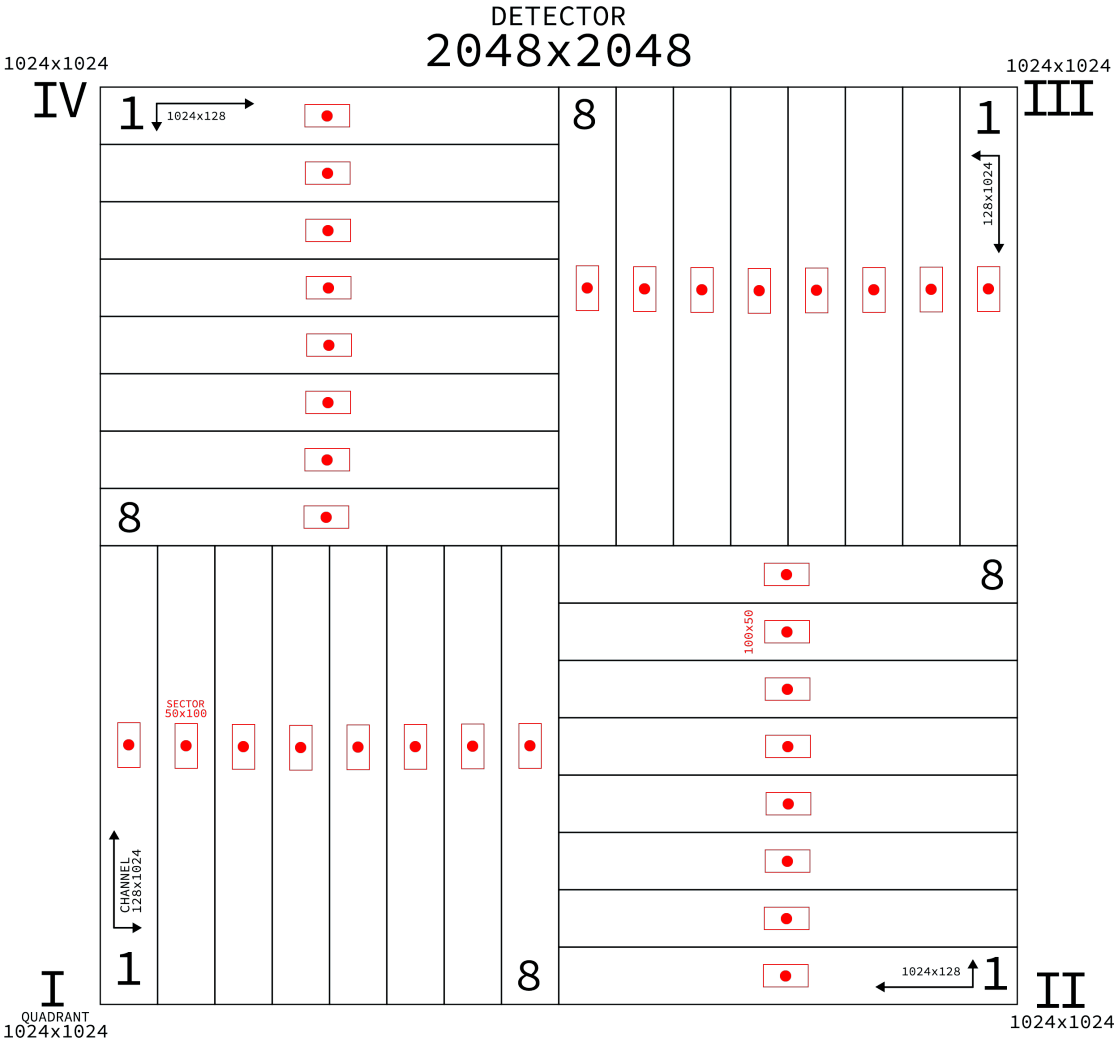

FIGURE 1.1: Detector scheme.

The arrows in each of the quadrants represent the detector reading. Each of the 32 channels shall be read simultaneously from the edge of the detector towards the centre of the detector in a clockwise direction. The short arrow is the fast axis that in each channel (and at the same time) reads one by one the 128 pixels of that row. It then switches to the next row of 128 pixels following the slow axis (the long arrow) until the total of 1024 rows is completed. In short, when we read a

pixel, we actually read 32 and follow the order already described by going through the detector panel [3].

In turn, we have fixed the central point of each channel, which will have a sector around it, as shown in the figure. These sectors will be used later on to extract the number of counts that we will use for our calculations and, to be able to analyse homogeneously, the complete surface of the detector, without handling an excessive volume of data.

1.3.1 Detector's readout modes

The way in which we obtain the data will be relevant since, due to the way in which the detector pixels are traversed in a readout, there can be a significant mismatch between the integration times between the different pixels of the same image. To avoid this, the detector has several readout modes, of which we will use 2 of them:

1. ***CDS:*** The detector pixels are accessed just after the reset and, after the integration time, read back. The result of the measurement will be the difference between the last image and the first one thus eliminating the mismatch of integration times between homologous pixels. This also eliminates the reset noise, but increases the readout noise by a factor of $\sqrt{2}$, and the frame rate will be greater than 1 second [4].

2. ***RAMP:*** Between each detector reset, the data is read several times and equispaced in time. This mode is suitable for longer integration times, the detector is able to reach steady state, so we get a better estimate of the flux received by calculating the slope of the measurement curve versus time [4].

It is important to define integration time as the time interval between the first reading of any pixel and the last reading of that pixel. It is also important to note the inclusion of non-productive readings (where no data is collected) whenever possible between measurements in order to keep the detector in a stable regime.

1.4 Objectives and general methodology

This work aims to calibrate the EMIR detector, so that we can obtain real measurements without being affected by the conditions in which the equipment is located or by factors inherent to the design of the instrument itself.

For this reason, this project is divided into several chapters, each of them related to a feature of the detector rather than of the target object itself, so they have to be removed. These features are: dark current, readout noise, linearity and the gain of the detector itself. This project will try to understand and measure each of these phenomena in order to take them into account when dealing with data from real observations.

The *a priori* method will be to take many images with the same configuration in order to justify a pattern by analysing the data obtained. In this way, having some statistics to back it up, the final contribution of each of these factors can be quantified.

In order to perform all these calculations, we will make use of a computer and develop several scripts in the programming language *Python* as required in each case.

Chapter 2

Dark Current and drift

In a detector there is always a certain conduction associated with the charges released due to thermal excitation. This produces a parasitic signal that will affect all measurements made. This phenomenon is known as dark current [5]. Although when doing broadband photometry, the emissivity of the sky is the dominant background source, when using EMIR to do spectroscopy outside of these emission regions of the sky, it is possible that the dark current will be the dominant signal source.

En un detector siempre hay una cierta conducción asociada a las cargas liberadas debido a la excitación térmica. Esto produce una señal parásita que afectará a todas las mediciones realizadas. Este fenómeno se conoce como corriente oscura [5]. Aunque cuando se hace fotometría de banda ancha, la emisividad del cielo es la fuente de fondo dominante, cuando se utiliza EMIR para hacer espectroscopia fuera de estas regiones de emisión del cielo, es posible que la corriente oscura sea la fuente de señal dominante.

2.1 Methodology

To analyse the dark current, we must ensure that no radiation is incident on the detector, so that when we take a series of readings, the dominant source of the signal is this radiation that we named dark current. Once enough time has elapsed for the detector to stabilise, the signal level we measure will then be the dark current [6].

Since we do not illuminate the detector, and the reset does not completely eliminate the eddy current, the signal we measure competes with the dark current. This results in a drift caused by the residual charge on the instrument's capacitors. Therefore, for integration times that are too short, we are not really measuring the dark current, but a drift in the signal because the detector has not yet reached its stable phase.

The experimental process will consist of taking 6 series of measurements of 10 sequences each with a rest interval of 3 minutes between each series. We will repeat this for different exposure times and reading modes according to the following table.

Readout mode	Exposure time (s)
CDS	1.5
CDS	3
CDS	4
CDS	5
CDS	6
CDS	7
CDS	8
CDS	9
CDS	10
CDS	11
CDS	12
CDS	13
CDS	14
CDS	15
RAMP (5 frames)	20
RAMP (5 frames)	30
RAMP (10 frames)	60
RAMP (28 frames)	360

TABLE 2.1: Measurements made to calculate the dark current

In the latter case, for measurements with 360 seconds of exposure, only 5 series have been taken instead of 6. From all the images obtained, we will extract the data (number of counts) in each of the channels using the sectors already described in the section corresponding to the figure 1.1. While users can also command integration times between 60 and 360 seconds, the detector readout scheme in all of these are the same than that in the 360 seconds case. So this readout can be used

to derive also the dark current pattern in shorter integration times.

We will plot each of the curves for all these measurements and perform a linear fit. The values of the slopes obtained will be the number of counts per second, i.e. the flux associated with the parasite current. This is taking into account the fact that for short integration times (the measurements in the *CDS* mode) what we are measuring will be a drift in the signal and not the dark current as such. It is important to take into account that the linear adjustment has been made with the second half of the points of each *RAMP* to guarantee the stable regime of the detector. In the case of *CDS* this is impossible as we only have 2 frames (points) per measurement.

The dark current, or drift value will be the average of all slope values for each sector in each case. Also is important to perform the corresponding error propagation. That is, the weighted average of the slopes:

$$\overline{x} = \frac{\sum_{i=1}^{N} w_i x_i}{\sum_{i=1}^{N} w_i} \tag{2.1}$$

Where the weights (w_i) used for the mean are the inverses of the variances:

$$w_i = \frac{1}{\sigma_i^2} \tag{2.2}$$

And the final error of all promediate results is:

$$\sigma_{total} = \sqrt{\frac{1}{\sum_{i=1}^{N} \frac{1}{\sigma_i^2}}} \tag{2.3}$$

Here we have an example of one of these measurements, in this case, we have a 28 frames *RAMP* and it belongs to the 3 series of measurements (imgobbl=3). The figure shows several subplots which represent each of the 32 channels that EMIR has. They are labelled with reference to the central pixel of the sector corresponding to each channel and the result they show is the arithmetic mean with its variance as the error of the 10 measurements taken consecutively in that series. In the upper margin, the weighted average (2.1), (2.2) of each of these results with his total error as (2.3).

FIGURE 2.1: *RAMP* 28 frames

2.2 Results and discussion

In order to be able to perform good statistics (with a larger volume of data in order to be more accurate), we have to check that the results between each series agree within their error. For this purpose, all measures have been analysed separately.

Imgobbl	1	2	3	4	5	6
CDS 1.5s	13.845 ± 0.9681	13.639 ± 0.9719	13.606 ± 0.9249	13.272 ± 0.9064	13.902 ± 0.8956	13.786 ± 0.9401
CDS 3s	11.398 ± 1.3982	11.363 ± 1.3975	11.256 ± 1.3999	11.192 ± 1.3763	11.389 ± 1.4016	11.482 ± 1.3852
CDS 4s	10.906 ± 1.4707	10.736 ± 1.4635	10.639 ± 1.4816	10.861 ± 1.4699	10.900 ± 1.5119	10.734 ± 1.4580
CDS 5s	9.925 ± 1.4750	9.896 ± 1.4604	9.959 ± 1.4602	9.914 ± 1.4674	9.905 ± 1.4716	9.910 ± 1.4692
CDS 6s	9.121 ± 1.4288	9.016 ± 1.4408	9.077 ± 1.4292	9.046 ± 1.4161	8.952 ± 1.4298	9.064 ± 1.4272
CDS 7s	8.311 ± 1.3796	8.286 ± 1.3827	8.239 ± 1.4007	8.336 ± 1.3856	8.301 ± 1.3758	8.229 ± 1.3728
CDS 8s	7.565 ± 1.3353	7.597 ± 1.3414	7.562 ± 1.3364	7.602 ± 1.3344	7.591 ± 1.3208	7.579 ± 1.3274
CDS 9s	7.093 ± 1.2815	6.991 ± 1.2653	7.002 ± 1.2770	7.067 ± 1.2795	7.013 ± 1.2769	6.969 ± 1.2683
CDS 10s	6.530 ± 1.2286	6.482 ± 1.2126	6.496 ± 1.2113	6.501 ± 1.2235	6.482 ± 1.2185	6.459 ± 1.2269
CDS 11s	6.059 ± 1.702	6.055 ± 1.1645	6.047 ± 1.1536	6.072 ± 1.1641	6.045 ± 1.1614	6.026 ± 1.1610
CDS 12s	5.670 ± 1.1142	5.693 ± 1.1097	5.651 ± 1.1169	5.698 ± 1.1206	5.626 ± 1.1210	5.607 ± 1.1040
CDS 13s	5.349 ± 1.0714	5.317 ± 1.0664	5.339 ± 1.10654	5.349 ± 1.0806	5.299 ± 1.0650	5.294 ± 1.0632
CDS 14s	5.005 ± 1.0252	4.961 ± 1.0134	4.979 ± 1.0145	5.003 ± 1.0265	4.985 ± 1.0266	5.008 ± 1.0245
CDS 15s	4.710 ± 0.9773	4.716 ± 0.9723	4.710 ± 0.9704	4.736 ± 0.9775	4.696 ± 0.9697	4.723 ± 0.9798
RAMP 20s	2.914 ± 0.3066	2.914 ± 0.3110	2.937 ± 0.3183	2.977 ± 0.3118	2.894 ± 0.3116	2.982 ± 0.3167
RAMP 30s	1.346 ± 0.1374	1.361 ± 0.1344	1.329 ± 0.1382	1.338 ± 0.1415	1.320 ± 0.1384	1.378 ± 0.1466
RAMP 60s	0.185 ± 0.0140	0.198 ± 0.0153	0.200 ± 0.0133	0.187 ± 0.0164	0.188 ± 0.0144	0.185 ± 0.0144
RAMP 360s	0.067 ± 0.0008	0.062 ± 0.0010	0.059 ± 0.0007	0.059 ± 0.0010	0.056 ± 0.0007	

TABLE 2.2: Dark current (or dirft) values for each series.

As we can see from table 2.2, in each case everything agrees within the error, so we can justify a simultaneous average of all the measurement series for each case. This result is shown below for the average of all of the 5 series of measurements with 28 frames *RAMP*:

FIGURE 2.2: All 28 frames *RAMP* series.

We have chosen the measurements *RAMP* with 360 seconds of integration because this way we have more data in the stable region of the detector and, therefore, a much more faithful value to the dark current.

It is important to mention the difference between having the detector in steady state or not, this can be seen in the rise of the first points of each curve and, in turn, the first ramps with respect to the last ones.

As the detector takes readings and is in operation, the more stable it becomes. These first values in each ramp show a large rise in the signal due to the residual charge on the capacitors after each reset. When measuring consecutively, these gaps in the non-stable region become more and more stable to the point where they no longer vary. It should be noted that in order to be able to make a comparison between all measurements, we have lowered the number of beads in the first point to an arbitrary value of 1000 beads. Thus shifting all ramps to the same level.

For this reason we have calculated the slope using only the second half of each ramp in each case. Due to the integration times used in *CDS*, we only have 2 frames (2 points) and the detector also does not reach its stable phase, which is where we can measure the dark current without taking into account the effects of the electronics inherent in the instrument.

Chapter 3

Readout noise

In the detector reading process, the charge captured in the resolution elements is queried, this charge is transformed into a current that carries the measurement information to the analogue-to-digital signal converter. This process will introduce variations in the current, associated with fluctuations in the detector electronics. This is due to the fact that the response of the detector components is not constant, resulting in the measurements made with the detector being affected by so-called readout noise [5].

En el proceso de lectura del detector se consulta la carga captada en los elementos de resolución, esta carga se transforma en una corriente que lleva la información de la medición al convertidor de señal analógica a digital. Este proceso introducirá variaciones en la corriente, asociadas a las fluctuaciones de la electrónica del detector. Esto se debe a que la respuesta de los componentes del detector no es constante, por lo que las medidas realizadas con el detector se ven afectadas por el llamado ruido de lectura [5].

3.1 Methodology

To analyse the read noise, we are interested in taking images in the absence of signal, as we did for the dark current. In this case, we want the detector to be as stable as possible, so we have decided to take the images with long exposure times, specifically we have a *RAMP* of 200 frames over 5589 seconds, which is more than

allowed at user level. All so that in the end the read noise component has more weight than the dark current in the measurement.

It should be noted that this ramp is divided into subgroups without any reset in between, all this so that the integration time is as long as possible and, therefore, to have the lowest possible signal where the dark current and the readout noise stand out. The *RAMP* that we have taken with 200 frames, we have done it with NLOOP=9 and NRDIL=20, that is to say, we repeat the *RAMP* 9 times more (making a total of 10). And in each repetition we make 20 readings (NRDIL). Thus we have a *RAMP* formed by 10 groups of 20 points without reset between reading groups.

In the previous chapter, we used the median of the data to perform the dark current calculation. This procedure (median) removes dead and hot pixels. In this case we will need the variances of the measurements so it is necessary to take the mean. To eliminate possible dead or hot pixels, we will select in the first reading (frame) of our sample, the pixels between 1000 and 10000 counts in each of the sectors already described in 1.1. These pixels will be the ones we will take for averaging when constructing the data matrices we will use in our calculations.

We will take two data arrays, one for each of the last two subgroups of our ramp, which is when the detector will be most stable and the data sets will be as similar as possible. We will make the variance of the difference of these two data arrays, to minimize the signal that may impinge on the detector despite being capped and where only the readout noise itself is measured:

$$Var(S_1(x,y) - S_2(x,y)) = \sum_{i=1}^{N} \frac{(S_1(x_i,y_i) - S_2(x_i,y_i) - \overline{S})^2}{N} \tag{3.1}$$

Where $\overline{S}$ is the average value of the signal.

We will use the square root of this value (3.1), i.e. the standard deviation of the signal difference in the last two subroups of our ramp, divided by two since we assume that the readout noise is an intrinsic parameter of the detector and is therefore equal over time. This will be our read noise:

$$\sigma_{RON} = \sqrt{\frac{Var(S_1(x,y) - S_2(x,y))}{2}} \tag{3.2}$$

3.2 Results and discussion

3.2.1 Evolution of the dark current

As we have already explained this parameter in the previous chapter, we will limit ourselves to show the data for dark current with even longer integration times. In addition, this way we verify the stable regime of the detector and the almost negligible contribution of the dark current for such long times.

In the figure below we can see how, although the number of reads increases with time, the slope of the curves (the dark current) is close to zero. In some cases, in the last points of each loop, the slope becomes negative due to the fluctuations of the detector and the very small value of dark current. For this calculation we have used the second half of points forming each loop of the *RAMP*.

In the following image we can clearly see each subgroup of points (each NLOOP). It is important to note that the x-axis does not represent time but simply the number of points. Also, 10 minutes elapse between each subgroup, but for reasons of space in the graph we have represented it like this. The set of subgroups will be ascending as there is no reset between each NLOOP and the detector continues to integrate.

FIGURE 3.1: Evolution of the dark current.

3.2.2 Readout noise

As we have already seen, the read noise equals the standard deviation (4.2) of the number of accounts.

	Quadrant 4	Quadrant 3
Channel	σ_{RON} ADU	σ_{RON} ADU
1	6.529	3.897
2	7.560	4.040
3	8.199	5.316
4	8.078	5.675
5	6.743	6.810
6	7.013	7.153
7	5.120	7.095
8	5.137	6.380
	Quadrant 1	Quadrant 2
Channel	σ_{RON} ADU	σ_{RON} ADU
1	4.167	3.062
2	4.748	3.822
3	5.894	5.403
4	6.814	5.208
5	7.097	6.459
6	8.105	7.072
7	8.335	7.202
8	8.117	6.519

TABLE 3.1: Readout noise

The mean value (4.1) for readout noise is:

$$\sigma_{RON} = 6.212 ADU \tag{3.3}$$

Chapter 4

Linearity

The dynamic range of our detector will be compromised by linearity. That is, the proportionality between the incident radiation flux and the output voltage of the detector. Determining the linear range of our detector is important to be able to make quality measurements, because as we approach the saturation level of the detector, the output voltage is no longer a faithful reflection of the incident light. In other words, a measurement outside the linear range of the detector will give us a series of false data [5].

El rango dinámico de nuestro detector se verá comprometido por la linealidad. Es decir, la proporcionalidad entre el flujo de radiación incidente y la tensión de salida del detector. Determinar el rango lineal de nuestro sensor es importante para poder realizar medidas de calidad, ya que a medida que nos acercamos al nivel de saturación del detector, la tensión de salida deja de ser un fiel reflejo de la luz incidente. Es decir, una medida fuera del rango lineal del detector nos dará una serie de datos falsos [5].

4.1 Methodology

To determine the linear range of the detector, we will take several ramps by illuminating the detector with a constant, homogeneous light source. In our case, we have taken 3 ramps with 30 frames each over an exposure time of 50 seconds.

In each case, we have ignored the first point of each ramp because of the spike it suffers from the reset voltage. Then, taking the second through the sixth point (a total of 5 points in all) we performed a linear fit and, with the values of the coefficients of the polynomial obtained, predicted the next point. By repeating this process we have made the ramp adjustment up to a given threshold.

This threshold is determined by us by imposing a tolerance level. That is, if the difference between the value predicted by the previous adjustment and the value measured at a given point in the ramp is greater than the tolerance level, that is the point where our detector changes from a linear to a non-linear regime. We have tested with tolerances at 1% and 2%. The average value between the first point outside the linear range and the last point inside the linear range will be the limit of the EMIR linear range [6].

As usual, we have done this in the central region of each of the 32 that make up the detector. We have made statistics of the results obtained by taking the mean value of the linearity as the arithmetic mean:

$$\overline{X} = \sum_{i=1}^{N} \frac{x_i}{N} \tag{4.1}$$

And the standard deviation:

$$\sigma = \sqrt{\frac{\sum_{i=1}^{N}(x_i - \overline{X})^2}{N}} \tag{4.2}$$

As the error.

4.2 Results and discussion

We have performed the method described above a total of 6 times, i.e. each of the 3 ramps with both levels of tolerances (1 and 2). Below is an example of what we have obtained:

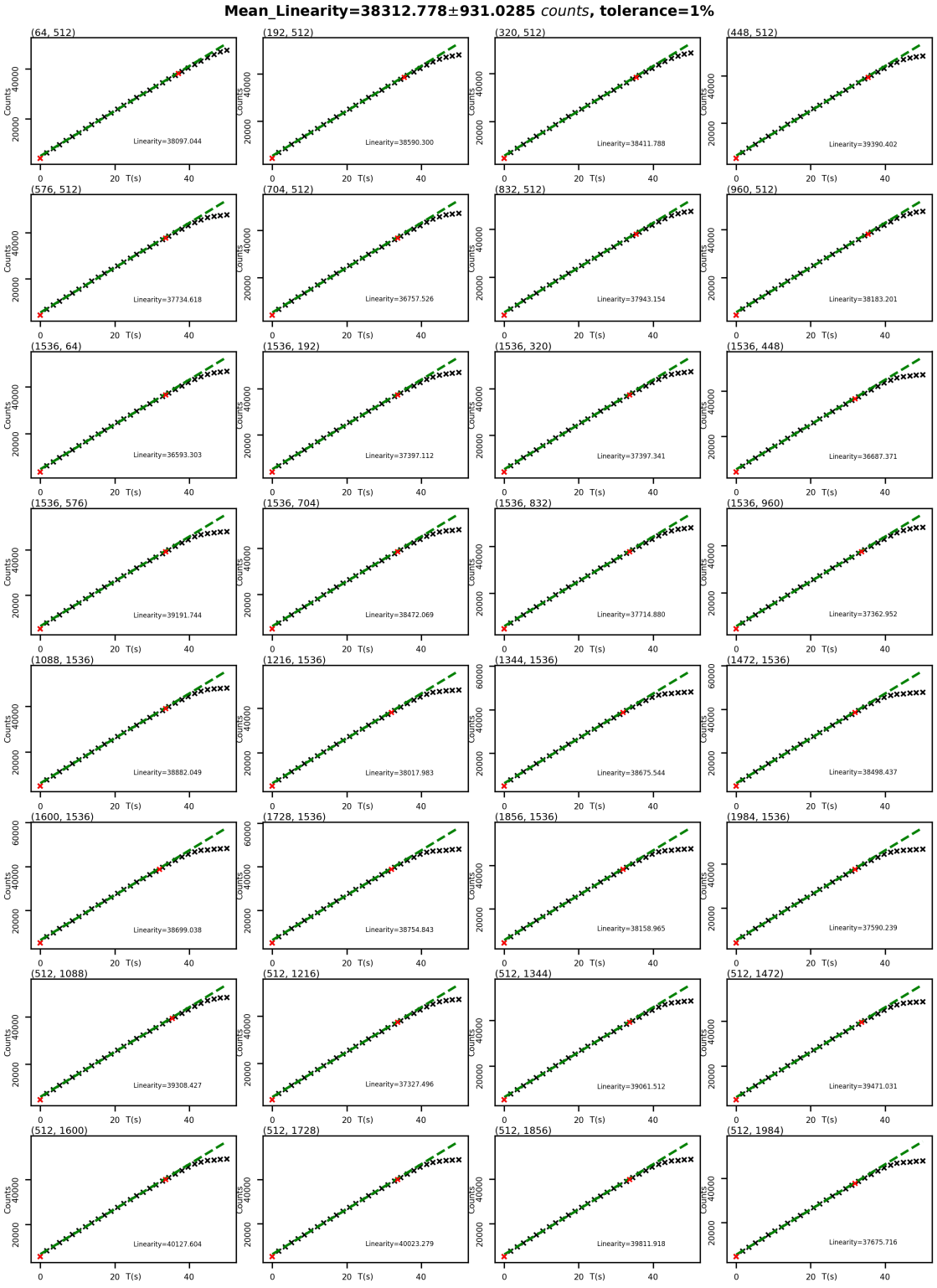

FIGURE 4.1: 3*rd RAMP* linearity with 1% tolerance.

In order not to make this document too long, we will present all the results in the following table:

Tolerance	*RAMP 1*	*RAMP 2*	*RAMP 3*	Weighted mean
1%	39463.569 ± 1008.4799	38140.051 ± 877.1662	38312.778 ± 931.0285	38607.315 ± 311.9436
2%	45446.574 ± 736.9034	45430.613 ± 815.1022	45437.778 ± 874.9812	45438.622 ± 268.3301

TABLE 4.1: Linearity range values (counts) for each *RAMP*

Where the weighted mean has been done using the equations (2.1), (2.2) y (2.3)

We can see that the results fit together within the errors obtained. Finally, we will stick with the most stringent value for the linear range of the detector, i.e. the one with a tolerance of 1%.

$$linearity = 38607.315 \pm 311.9436(counts) \tag{4.3}$$

Chapter 5

Detector gain

The incidence of photons on the detector causes it to emit electrons (photoelectric effect). These electrons generate a current that can be measured, which is the basis of the measurements made in EMIR or any other similar detector. These currents are quite slight, so they are amplified and transformed into a digital signal in order to ensure their transmission through the system's circuitry [5]. This digital signal will be the final result of the measurements made by the system.

La incidencia de los fotones en el detector hace que éste emita electrones (efecto fotoeléctrico). Estos electrones generan una corriente que se puede medir, que es la base de las mediciones realizadas en EMIR o en cualquier otro detector similar. Estas corrientes son bastante leves, por lo que se amplifican y se transforman en una señal digital para asegurar su transmisión a través de los circuitos del sistema [5]. Esta señal digital será el resultado final de las mediciones realizadas por el sistema.

5.1 Methodology

We will use the same measurements and calculations made in the linearity chapter. In this case we have made sure that we are within the linear range by using only those points of the ramp with a number of counts between 1000 and 10000 counts.

The variance of the signal and the inverse of the detector gain are linearly related as follows:

$$Var_S(ADU) = \frac{S(ADU)}{g} + Var_n(ADU) \tag{5.1}$$

Where the independent term $Var_n(ADU)$ refers to any other noise source present at the time of measurement. When we have high values of signal flux S we minimize the importance of this independent term so we can assume $Var_n(ADU) \approx 0$. It is important to note that these values must be used in *ADU (analog to digital unit)*.

The gain calculation consists of taking the data from 2 different ramps and take the variance of the difference of the two ramps (3.1). We do this to remove the signal value in the measurements and keep only the signal fluctuations since our detector follows a poisson statistic. We will ensure to use pixels that are within our linear range imposed earlier.

As we took the difference between two ramps and then did the variance for the results obtained, we will average the sum of these two ramps. It must be taken into account that as the signal source has been the same in both measurements, we will have to divide the average of this sum of ramps by two. In this way, we obtain a more accurate average:

$$< S(x,y) >= \frac{< S_1(x,y) + S_2(x,y) >}{2} \tag{5.2}$$

We then perform a linear fit of this variances against the averaged signal and, finally, the slope of this line will be the gain g of our detector. We will take the mean (4.1) of the gain in each of the 32 channels as the total value of the gain g its standard deviation (4.2) as its error.

5.2 Results and discussion

In our case, as we have 3 ramps we have seen that the best possible combination is the last 2, since the first of them presents peaks in the signal in the signal in some pixels and, as the number of counts increases, the average value of the gain will be compromised. This is because the detector has not had time to reach the stable regime that we have already discussed above, remembering that the longer

the detector is in use, the more stable it is (this is better explained in the chapter on dark current).

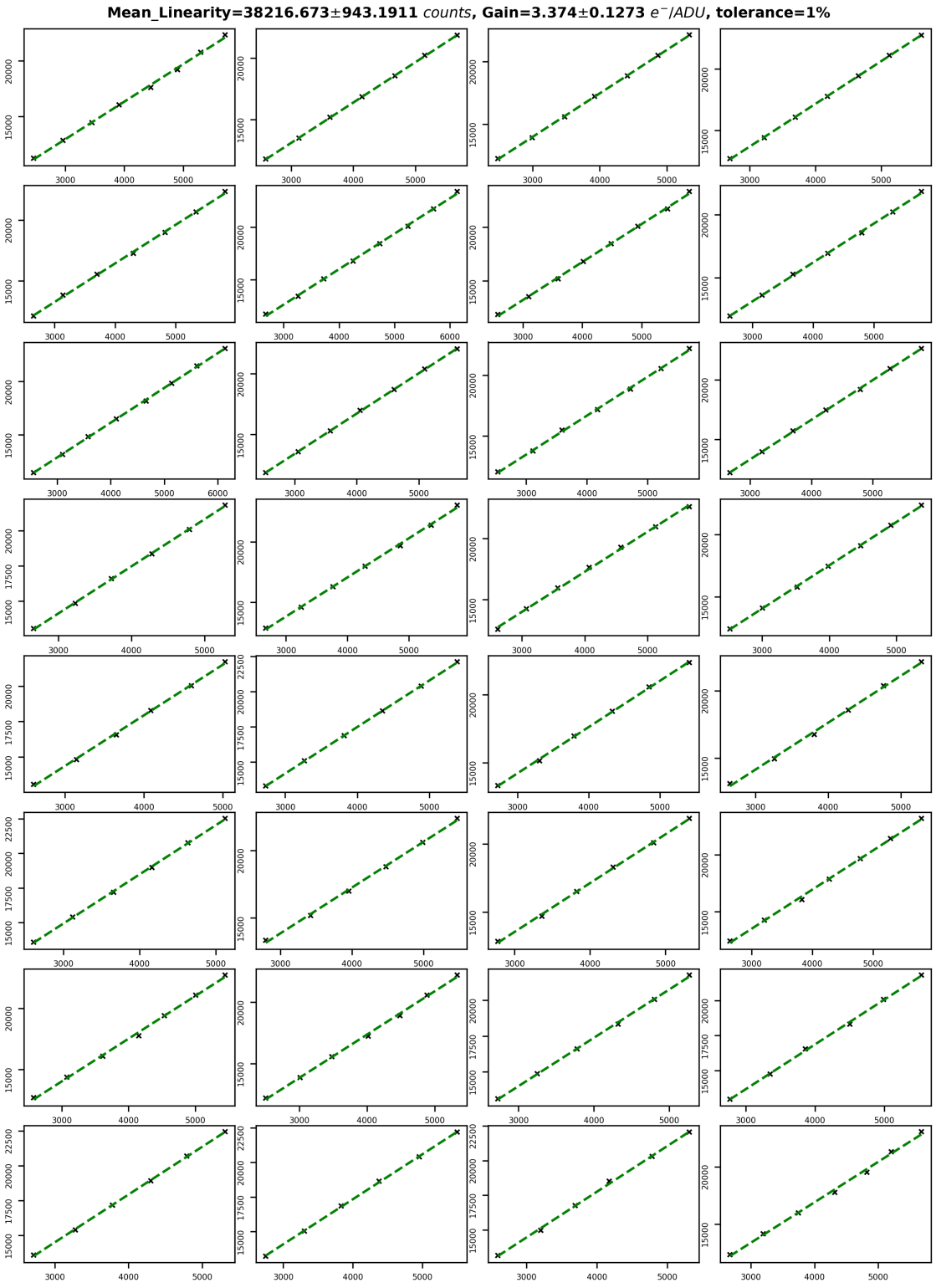

FIGURE 5.1: Linear fit for the gain of the average of the last 2 *RAMPs*

As we can see we have the following value for the gain:

$$g = 3.374 \pm 0.1273 \frac{e^-}{ADU} \tag{5.3}$$

Which is in agreement with that obtained years ago by the calibration work carried out by Carlos González in his thesis [6].

Chapter 6

Conclusions

In this final chapter we will compare our results with those obtained in Carlos González's doctoral thesis [6], draw some conclusions about the detector in general and make a number of suggestions for possible future work as a continuation or extension.

En este capítulo final compararemos nuestros resultados con los obtenidos en la tesis doctoral de Carlos González [6], sacaremos algunas conclusiones sobre el detector en general y haremos una serie de sugerencias para posibles trabajos futuros como continuación o ampliación.

6.1 Results

In this work we have characterised the detector by calculating the fundamental parameters of the detector. The data we used were provided by the IAC, a total of 5786 images with which we performed the calculations and developed our methodology.

For this we have elaborated a series of scripts in *python*. At first we learned how to use the *astropy* library to handle files in *".fits"* format. This file format has, on the one hand, the image itself and, on the other hand, the header with all the information and metadata of the image. By accessing the header we can extract information about the way the image was taken, this has allowed us to order the images of each *RAMP*, to obtain the exposure time in each case and other relevant information.

Knowing how to handle the files, we proceeded to perform the calculation for each of the parameters of the detector in the same order as this work is presented. Although we have followed somewhat simpler methods to characterise the detector, we have obtained good results within expectations. Comparing with the work of González-Fernández in 2010 [6], we can see differences in some results which we are going to review.

In the case of the readout noise where, despite obtaining a different value, at least it remains in the same order of magnitude. We obtained $\sigma_{RON} = 6.212$ ADU and González-Fernández obtained [6] $\sigma_{RON} = 1.99$ ADU, but this result comes from the fitting over the ramp.

In the case of the dark current we obtain very close values although they do not quite fit within the margin of error, this may be due to the differences in methodology between the studies or the data used. We obtained $dc = 0.063 \pm 0.0003$ ADU/s and González-Fernández [6] $dc = 0.084 \pm 0.006$ ADU/s.

For the gain we have obtained practically the same result as they fit each other within the calculated margin of error: We obtained $g = 3.374 \pm 0.1273(\frac{e^-}{ADU})$ and González-Fernández [6] obtained $g = 3.02 \pm 0.16(\frac{e^-}{ADU})$.

Finally, in the case of the correction to the detector linearity, we have made the adjustment using different tolerances. In our case we have used a tolerance of 1% and González-Fernández [6] have used a tolerance of 2%. So it does not make sense to compare both results.

6.2 Observations

It is clear that EMIR is a versatile instrument and a novelty in its field. We have parameterised the main sources of noise that can contaminate the signal obtained by the detector during an observation. Thanks to this, we can obtain high quality data, especially for the study of distant galaxies at redshift beyond $z = 2$.

EMIR will serve as a bridge between the technical capabilities of today's spectroscopy and those that will emerge in the coming decades. In addition, it will also help to connect the near-infrared galaxy surveys carried out in the 1990s with those planned for beyond $z = 6$ in the near future.

6.3 Proposals for the future

Firstly, it would be good to repeat the work, making sure to use the same data that Fernández-González used in 2010 [6], so that we can determine if the differences between his methodology and ours have an important weight that can be reflected in the results.

It would also be interesting to look for similar calibration and characterisation work on other detectors of the same type in order to compare results.

Another suggestion for a possible future work is to reproduce Carlos's exact methodology but using more current data and see if the passage of time and the use of the detector over the years influences these values.

Finally, other parameters that we could not cover in this work remain to be calculated. Such as: the quantum efficiency of the detector, the cosmetics (inhomogeneities in the pixel response, fringe patterns or biases in the least significant bit) or the effect of instrument temperature cycling on the detector.

Bibliography

[1] Francisco Garzón et al. *EMIR user's manual*. IAC, 2020.

[2] Francisco Garzón. *EMIR instrument description*. IAC, 2006.

[3] Fernando Gago Rodríguez. *Driving the HAWAII-2 detector*. IAC, 2001.

[4] Francisco Garzón. *Detector readout modes on verification at system level*. IAC, 2015.

[5] Ian S. McLean. *Electronic imaging in astronomy: Detectors and instrumentation*. Springer, 1997.

[6] Carlos González Fernández. *Estudio espectrofotométrico del interior galáctico: Un proyecto para EMIR*. Tesis doctoral ULL, 2010.